AGU PUBLICATIONS

JGR

Journal of Geophysical Research: Space Physics

RESEARCH ARTICLE
10.1002/2017JA024536

Modeling, Analysis, and Interpretation of Photoelectron Energy Spectra at Enceladus Observed by Cassini

S. A. Taylor[1,2], A. J. Coates[1,2], G. H. Jones[1,2], A. Wellbrock[1,2], A. N. Fazakerley[1], R. T. Desai[1,2], R. Caro-Carretero[1,3], M. W. Michiko[4], P. Schippers[5], and J. H. Waite[6]

[1]Mullard Space Science Laboratory, University College London, Dorking, UK, [2]The Centre for Planetary Sciences at UCL/Birkbeck, London, UK, [3]Escuela Técnica Superior de Ingeniería - ICAI, Universidad Pontificia Comillas, Madrid, Spain, [4]Swedish Institute of Space Physics (IRF), Uppsala, Sweden, [5]LESIA, Observatoire de Paris, Meudon, France, [6]Southwest Research Institute, San Antonio, TX, USA

Abstract The Electron Spectrometer (ELS) of the Cassini Plasma Spectrometer has observed photoelectrons produced in the plume of Enceladus. These photoelectrons are observed during Enceladus encounters in the energetic particle shadow where the spacecraft is largely shielded from penetrating radiation by the moon. We present a complex electron spectrum at Enceladus including evidence of two previously unidentified electron populations at 6–10 eV and 10–16 eV. We estimate that the proportion of "hot" (>15 eV) to "cold" (<15 eV) electrons during the Enceladus flybys is ≈ 0.1–0.5%. We have constructed a model of photoelectron production in the plume and compared it with ELS Enceladus flyby data by scaling and energy shifting according to spacecraft potential. We suggest that the complex structure of the electron spectrum observed can be explained entirely by photoelectron production in the plume ionosphere.

Key Points:
- Plume photoelectron production can be modeled using the solar spectrum, photoionization interaction cross sections and plume neutral densities
- Background subtraction reveals a complex structure at low energies, including two previously unidentified photoelectron peaks
- We show qualitatively that the observed photoelectron spectrum near Enceladus can be explained entirely by plume photoelectrons

Correspondence to:
S. A. Taylor,
s.taylor.14@ucl.ac.uk

Citation:
Taylor, S. A., Coates, A. J., Jones, G. H., Wellbrock, A., Fazakerley, A. N., Desai, R. T., … Waite, J. H. (2018). Modeling, analysis, and interpretation of photoelectron energy spectra at Enceladus observed by Cassini. *Journal of Geophysical Research: Space Physics*, *123*, 287–296. https://doi.org/10.1002/2017JA024536

Received 30 JUN 2017
Accepted 22 DEC 2017
Accepted article online 3 JAN 2018
Published online 12 JAN 2018
Corrected 22 MAY 2018

This article was corrected on 22 MAY 2018. See the end of the full text for details.

1. Introduction

Photoionization is the physical process where a neutral atom or molecule becomes ionized by the interaction with a photon producing a photoelectron and a positive ion. The photoelectrons produced in this process have well-defined energies that correspond to the energy difference between the incoming photon and the ionization potential of the neutral atom or molecule (Huebner et al., 1992). In our solar system, the Sun provides the extreme ultraviolet photons required to produce photoelectrons and they are present wherever neutral atoms and molecules are found. Photoionization is a key ionospheric process at every body with an atmosphere, and photoelectrons have been measured directly by spacecraft at Earth (Coates et al., 1985), Venus (Coates et al., 2008), and Mars (Frahm et al., 2006). Since the arrival of Cassini at Saturn, photoelectrons have been observed in the Saturnian ring exosphere (Coates et al., 2005), Titan (Coates, Crary, Young, et al., 2007; Wellbrock et al., 2012), throughout the inner magnetosphere (Schippers et al., 2009) and in the plume of Enceladus (Coates et al., 2013; Ozak et al., 2012). A comparison of photoelectrons at Earth, Mars, Venus, and Titan was presented by Coates et al. (2011).

The energy spectra of solar system photoelectrons often exhibit a number of unique features. Pronounced peaks in the 20–30 eV energy range have been observed in many planetary atmospheres and are associated with the ionization of neutrals by the strong He II 30.4 nm solar emission line. The particular electron energy spectrum observed in an atmosphere depends on the neutrals present and the branching ratios for each photoionization reaction (Mantas & Hanson, 1979). Another feature is an observed dropoff of photoelectron production above ≈60 eV which is due to a reduction in solar photon intensity at wavelengths below 16 nm (Coates et al., 2011; Galand et al., 2006).

Saturn's inner magnetospheric region extends from the edge of the main rings to $\approx 6\,R_S$ ($1\,R_S = 1$ Saturn radii $\approx 60,268$ km) (Arridge et al., 2011). The magnetic field is dominated by the planetary internal field and is strongly dipolar throughout the region. The inner magnetosphere is immersed in an extended cloud of neutral gas. This gas is chemically coupled to the ion plasma, and its density exceeds that of the local plasma by at least an order of magnitude (Jurac & Richardson, 2007). This neutral gas has been measured by Cassini's Ion and Neutral Mass Spectrometer (INMS) (Perry et al., 2010) and the Ultraviolet Imaging Spectrometer (Esposito et al., 2005) and is composed mainly of H_2O and its dissociation products. Cold plasma is supplied

by a number of different processes including photoionization, charge exchange, and electron impact ionization. It is mostly confined to the equatorial plane leading to a corotating cold plasma torus (André et al., 2008). Warm electrons, some of which are produced by photoionization (Coates et al., 2013), may provide an important ionization source in the inner magnetosphere (Fleshman et al., 2012). Saturn's radiation belts are most intense in the inner magnetosphere, and so in addition to neutrals and cold plasma, the region is populated by trapped energetic (MeV) particles (Krupp et al., 2009; Paranicas et al., 2010).

Enceladus is Saturn's sixth largest moon with a radius of R_{En}=252 km. It orbits well within the inner magnetosphere and radiation belts at 3.95 R_S. Enceladus was identified as the primary source of the neutrals in the inner magnetosphere with the discovery of active venting from the moon's south pole which resulted from Cassini observations (Dougherty et al., 2006).

Plumes of neutral particles (Waite et al., 2006) and micron-sized icy dust particles (Spahn et al., 2006) have been discovered emanating from "tiger stripe" features on the icy surface at high southern latitudes (Porco et al., 2006). Significant quantities of these neutral particles become charged, and Cassini has detected plasma (Tokar et al., 2006, 2009) (including water group ion clusters; Coates et al., 2010) and charged nanograins (Hill et al., 2012; Jones et al., 2009) in the plumes.

In this paper we present further study of the "magnetospheric" and "plume" photoelectrons identified by Schippers et al. (2009) and Coates et al. (2013). In particular, inside the region shielded from energetic particles by Enceladus itself, we separate the photoelectrons from the background electrons and identify a multiple-peak structure which is present in both the magnetospheric and plume photoelectrons. A post hoc Wilcoxon signed rank (WSR) (Gibbons & Chakraborti, 2011; Sprent & Smeeton, 2016) nonparametric test of paired comparisons, using a normal approximation method, indicates that there are no statistically significant differences between the modeled background distribution and the Electron Spectrometer (ELS) data. We compare the subtracted ELS energy spectra from the E9 and E19 Enceladus flybys with a model of the plume photoelectron production rate. In addition to the two previously identified photoelectron peaks, we identify further low-energy photoelectron energy structure and study ratios between the two main peaks (C and D).

2. Instrumentation and Flyby Orientations

2.1. CAPS-ELS

The data used in this study come from the Cassini Plasma Spectrometer (CAPS) (Young et al., 2004)-Electron Spectrometer (ELS) (Linder et al., 1998), a hemispherical top hat electrostatic analyzer. Electrons enter the instrument and pass between concentric hemispherical electrostatic analyzer plates before hitting an annular microchannel plate detector. ELS measures electrons in an energy range of 0.6–28,000 eV/q with an energy resolution of 16.7%. The total angular coverage is 160° by 5.2° split equally between eight anodes in which each has angular coverage of 20° by 5° orientated about the spacecraft's X axis. The field of view is further increased by the rotation of the actuator CAPS that is mounted on which allows rotation by ± 100° (Young et al., 2004). Throughout this study we have considered data primarily from central anodes between 3 and 6 which have less obstructed fields of view than the edge anodes. CAPS was operational from the beginning of the mission to June 2011 and then from March to June 2012.

2.2. Flyby Geometry

There are 17 Enceladus flybys for which CAPS data are available. The trajectories of these flybys vary (some significantly) which allows us to investigate different aspects of Enceladus's local environment.

We use four classifications to describe the orientation of each Enceladus encounter: upstream, north-south, southern and northern. Figure 1 shows the geometry of a flyby from each of these classifications. These trajectory plots use an Enceladus-centered coordinate system: The X coordinate points along Enceladus's orbital motion, Y points toward Saturn, and Z is aligned with Enceladus's rotation axis and completes the right-handed set.

The format of these plots is as follows: Figure 1a shows the view down onto the northern pole of Enceladus, the corotation wake is in $+X$, and Saturn is off to $+Y$. Figure 1b shows the view in Enceladus's orbital plane with Saturn in the background. The corotation wake is again in $+X$, and the plume extends in $-Z$, south of the moon. Figure 1c shows the final projection, the view along the corotation wake with Saturn off in $+Y$ and the plume again extending in $-Z$. The arrows on each trajectory line show the direction the spacecraft traveled.

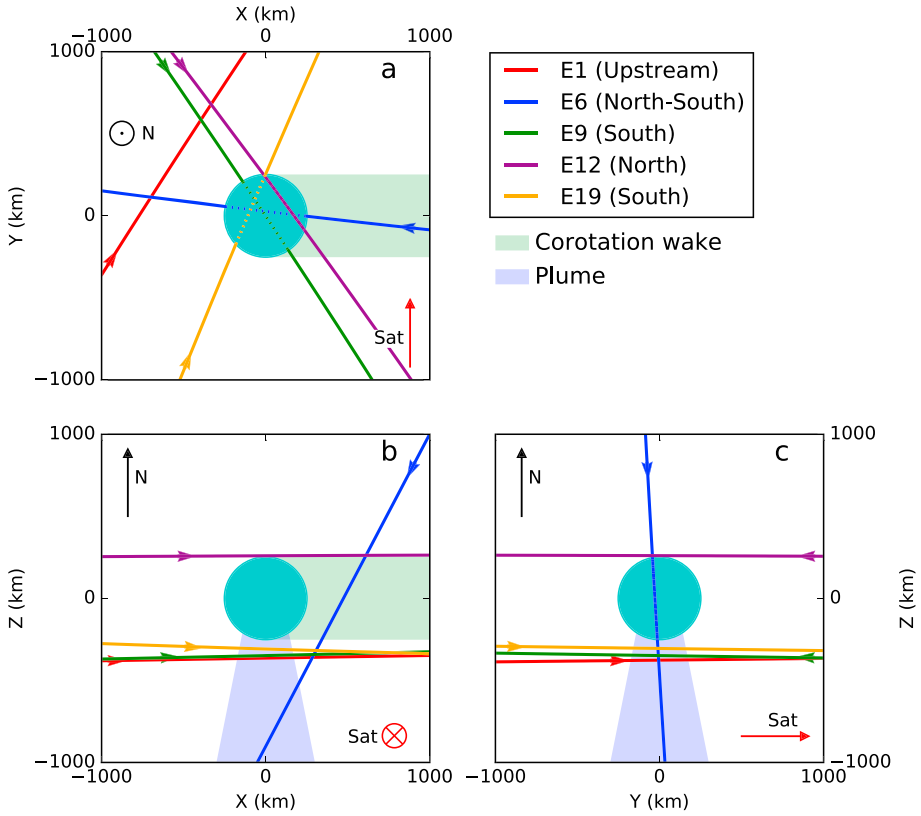

Figure 1. (a–c) Plots showing typical geometry of each flyby trajectory classification. The green-shaded region shows the nominal location of the corotation wake, and the blue-shaded region shows the region directly south of the disk of Enceladus where the plume is directly encountered.

E1 was an encounter in which the spacecraft passed upstream of Enceladus, not passing directly north or south of the disk of the moon. E6 was a north-south encounter in which the spacecraft crossed through the corotation wake from the north to the south before passing to the south of the disk. E9 and E19 were southern encounters during which the spacecraft crossed directly south of the disk.

During this study we examined data from a number of flybys across each classification and selected two flybys for further analysis. The selection criteria for choosing flybys suitable for investigating photoelectrons at Enceladus are as follows: The closest approach is within 2 R_E, and the ram angle is large (i.e., the instrument is pointing away from the ram direction so dust and negative ions are not measured; Coetes et al., 2010; Jones et al., 2009). Applying these criteria leaves us with flybys E1, E2, E6, E9, E12, E13, and E19 (see Table 1 in Coetes at al, 2013 for further information on each Enceladus flyby where CAPS data are available). We go on to analyze E9 and E19 in further detail by comparing the data to a plume photoelectron model. As well as satisfying the previous conditions, these southern flybys are most suitable for analyzing the plume because they pass through it horizontally and the distance to the surface does not vary significantly over the flyby. The other flyby classification which encounters the plume is north-south crossings during which the distance to the surface varies considerably throughout the encounter and as such is a much more complicated situation to analyze.

3. Observations

In Figures 2a and 2c, we show an energy time spectrogram for Enceladus flybys E9 and E19, respectively. A thermal magnetospheric electron population is visible across the spectrogram of both flybys at measured energies below ≈8 eV. We note a high count rate across all energies before and after the flyby caused by penetrating radiation. This penetrating radiation is primarily caused by energetic electrons (> 800 KeV) penetrating the 1.6 mm aluminum thick instrument shielding (Rymer et al., 2001). In the center of the plots there are significant drops in the count rate which we call the energetic particle shadow. This is caused by penetrating

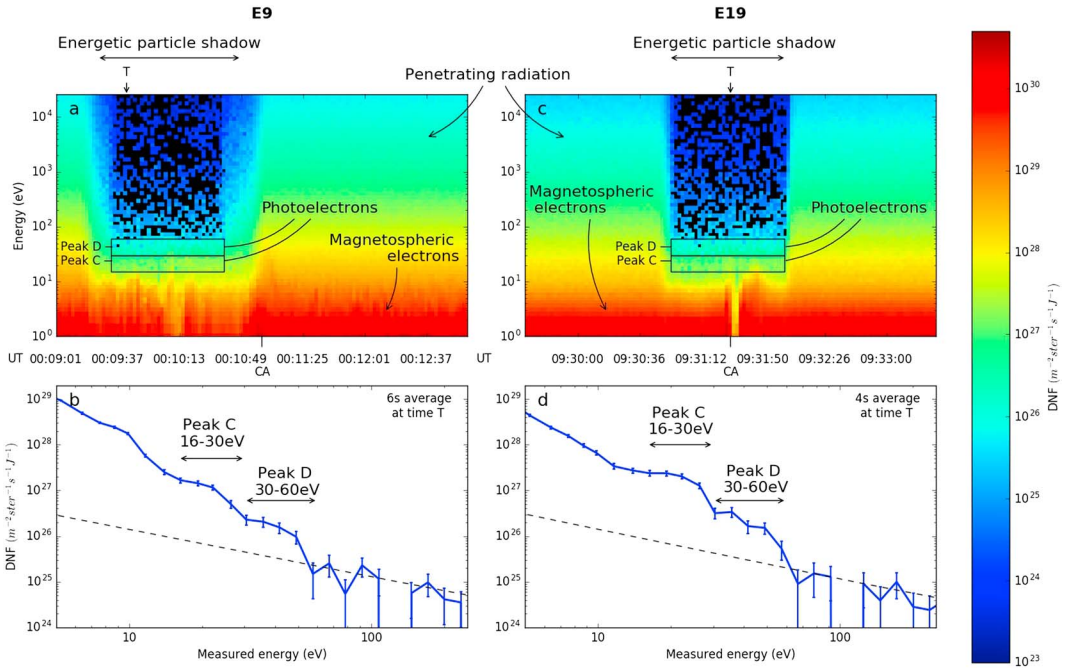

Figure 2. ELS data from the E9 and E19 Enceladus flybys. (a) Energy spectrogram across the E9 flyby. (b) Eight second averaged (four spectra) differential number flux (DNF) spectrum centered at 00:09:38 UT (time *T* indicated in Figure 2a). (c) Energy spectrogram across the E19 flyby. (d) Eight second averaged (four spectra) DNF spectrum centered at 09:31:27 UT (time *T* indicated in Figure 2c). Two energy peaks, C and D, are labeled. The dashed line indicates the single count level.

radiation being absorbed by the moon and the plume (Jones et al., 2006). The energetic particle shadow allows the observation of a number of features during the flyby including the presence of photoelectrons throughout the flyby produced by the ionization of neutrals both in the Enceladus plume (Coates et al., 2013) and throughout the inner magnetosphere (Schippers et al., 2009). There are two populations labeled "photoelectrons": Peak C at 16–30 eV and Peak D at 30–60 eV (these will be compared to similarly labeled model peaks later in the paper).

During the energetic particle shadow of E19 (Figure 2a) there are a number of interesting features in the magnetospheric electron population around closest approach. There is a sharp reduction in the magnetospheric electrons (< 8 eV) which is thought to be caused by attachment to ice grains in the plume (Coates et al., 2013). This feature is very well defined as the grains in the plume form a highly collimated beam (radius $\approx 1\ R_E$), while the neutral gas spreads out much further (Dong et al., 2015; Hill et al., 2012). Either side of this feature, there appears to be energy shifts in this population thought to be due to sharp spacecraft potential changes (Coates et al., 2013).

Figures 2b and 2d show an energy spectrum at time *T* in each respective spectrogram. Peaks C and D are the same as labeled in Figures 2a and 2c and are interpreted as photoelectrons (Coates et al., 2013; Schippers et al., 2009). These photoelectrons are a combination of both magnetospheric photoelectrons (generated from neutrals in the magnetosphere) and plume photoelectrons (generated from neutrals in the plume). Close to the plume, where the neutral density is high, there is a sharp increase in the total photoelectron flux due to the local production of plume photoelectrons. The peaks are reminiscent of photoelectron peaks appearing in modeled plume electron fluxes by Ozak et al. (2012). Peak C is associated by photoionization from the strong He II solar emission line at 30.4 nm. In other environments such as at Titan, the peak is relatively sharp in contrast to Enceladus where the peak is broad and exhibits a complex structure.

In order to further characterize these observed photoelectron peaks, we must first attempt to subtract the background magnetospheric electron population. Kappa distributions have been widely used to describe the velocity distributions of space plasmas throughout the solar system (Collier & Hamilton, 1995; Schippers et al., 2008; Vasyliunas, 1968). In Saturn's inner magnetosphere, it has been shown that a double-Kappa distribution can be used to represent the magnetospheric electron population (Schippers et al., 2008). In the case of

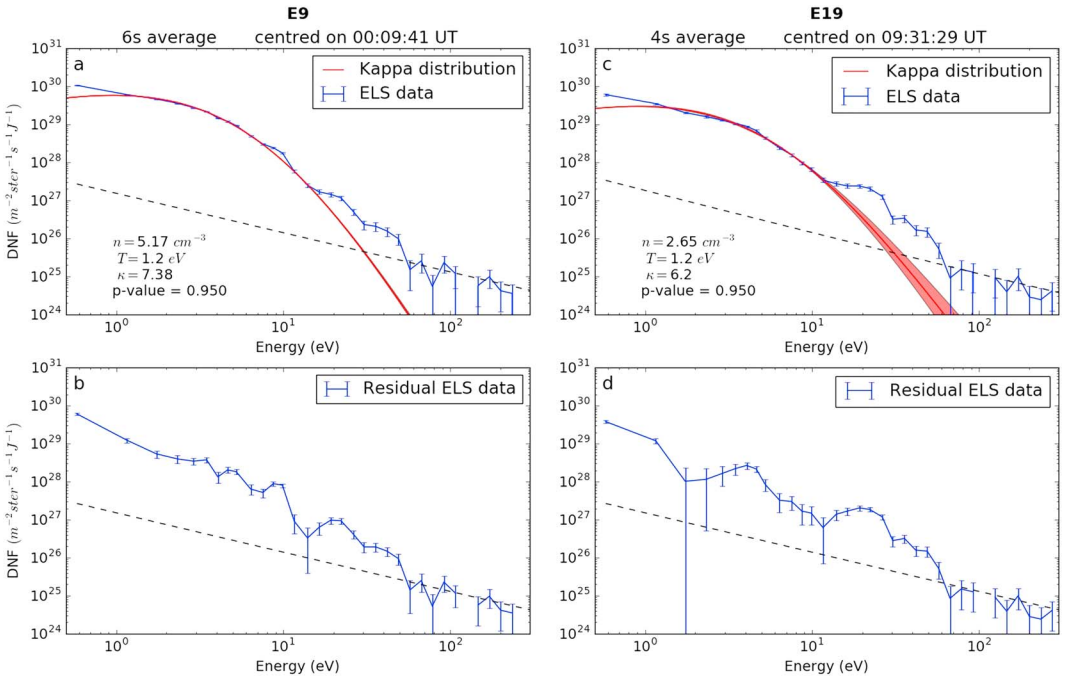

Figure 3. Kappa distribution and subtraction from E9 and E19 data. (a) Differential number flux spectrum of ELS data taken during Enceladus flyby E9 at 00:09:41 UT is shown in blue with a Kappa distribution fitting overlaid in red. (b) Residual differential number flux after Kappa distribution contribution is subtracted. (c) Differential number flux spectrum of ELS data taken during Enceladus flyby E19 at 09:31:29 UT is shown in blue with a Kappa distribution fitting overlaid in red. (d) Residual differential number flux after Kappa distribution contribution is subtracted. The dashed line in each panel indicates the single count level of ELS.

ELS data during the Enceladus flybys, we can fit a single Kappa distribution in order to subtract the magnetospheric population. It is not possible to fit a second Kappa distribution due to limited counts at high energies (>100 eV).

Figure 3 shows the results of applying the Kappa subtraction to the ELS data averaged over 6 and 4 s during the energetic particle shadows of E9 and E19. Figures 3a and 3c show the Kappa distribution fit plotted alongside the ELS data. Figures 3b and 3d show the residual flux once the Kappa distribution has been subtracted. We apply a post hoc WSR nonparametric test, using a normal approximation method to test the equality of the measured data and the fitted Kappa distribution function. The WSR test was chosen to assess the statistical significance due to its suitability in testing small sample sizes. A p value > 0.05 indicates that there are no statistically significant differences between the measured data and the fitted Kappa distribution function. The p values associated with the statistical tests for each of these fits indicate a good fit in each case.

4. Model

In order to investigate these electron populations, we construct a synthetic photoelectron production spectrum based on the modeling technique described by Schippers et al. (2009) to model photoelectrons in Saturn's neutral torus. We have adapted the method to model the production of photoelectrons in the plume by choosing five dominant neutral species found within the Enceladus plume by INMS and their mixing ratios (%) (Waite et al., 2017): 97.5 H_2O, 0.55 CO_2, 0.20 CH_4, 0.9 H_2, and 0.85 NH_3.

We consider each photoionization reaction listed for each of these species in Huebner et al. (1992). For each reaction within each considered species i we multiply the solar photon flux at Saturn $\Phi(\lambda)$ and reaction photoionization cross section $\sigma(\lambda)$ (taken from Huebner et al. (1992)). We then multiply this by its relative density in the plume n to find the production rate of each reaction R and sum each contribution to generate a total photoelectron production spectra (equation (1)).

$$R_i(\lambda) = \Phi(\lambda)\,\sigma_i(\lambda)\,n_i \tag{1}$$

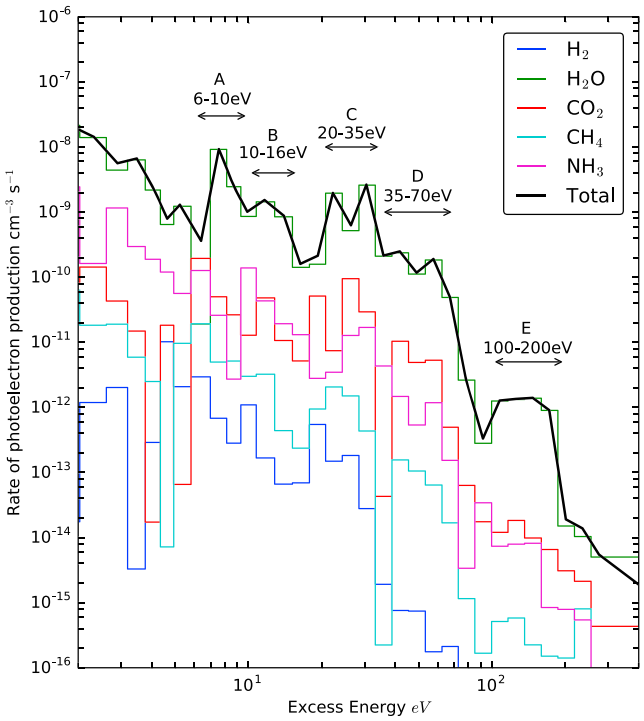

Figure 4. Synthetic photoelectron production (cm^{-3} s^{-1}) of H_2 in blue, H_2O in green, CO_2 in red, CH_4 in cyan, NH_3 in purple, and overlaid in black is the total combined production versus excess energy E_e ($E_e = hc/\lambda - \varphi$, where λ is the photon wavelength and φ is the threshold ionization energy). Photoelectrons in the energy range shown are produced by the solar spectrum photons with wavelengths between ≈3 and 62 nm.

The resulting synthetic spectrum corresponds to photoelectron production and does not include loss and transport processes. Due to the high neutral density in the plume, it is likely that electron neutral cooling is the main loss mechanism for these freshly produced photoelectrons. We do not expect any loss or transport processes to significantly alter the peak structure observed, and so we have considered only the photoelectron source in this simple model.

Figure 4 shows the modeled photoelectron production rate plotted against the excess energy E_e of the produced photoelectrons ($E_e = hc/\lambda - \varphi$, where λ is the photon wavelength and φ is the species binding energy). As H_2O is the dominant neutral species in the plume, it is the dominant source of photoelectrons in the model at almost all energies. The other species in the model (CO_2, CH_4, H_2, and NH_3) contribute mostly toward broadening the peaks. First, modeled peaks C (20–35 eV) and D (35–70 eV) are directly comparable to the peaks labeled C and D in Figure 2. The energy difference between these two sets of peaks is likely explained by spacecraft potential, and we will correct for this in analysis later in this paper. In addition to these two previously identified prominent peaks, there are three more peaks: A (6–10 eV), B (10–16 eV), and E (100–200 eV). We also see a sharp reduction in photoelectron production above ≈ 60–80 eV which is reminiscent of photoelectron observations made throughout the solar system (Coates et al., 2011).

Primarily considering the photoionization reactions of the most dominant neutral contributor, H_2O (binding energies of 12.6 eV, 18.1 eV, and 18.7 eV), we can trace the solar photon wavelength ranges responsible for each of the peaks: Peak A (6–10 eV) is formed due to photoionization by solar photons at wavelengths between 44–69 nm, Peak B (10–16 eV) by 36–56 nm photons, Peak C (20–35 eV) by 23–39 nm photons, Peak D (35–70 eV) by 14–23 nm photons, and Peak E (100–200 eV) by 5.7–11 nm photons. The other minor neutral species have similar binding energies, and so they contribute photoelectrons of similar wavelengths, only modified by a few nanometers.

5. Analysis and Discussion

We observe the photoelectron peaks at 16–30 eV (Peak C) and 30–60 eV (Peak D) across a variety of flybys with different encounter trajectories. In order to investigate the effects of the trajectory geometry on the measured photoelectron populations, we compare the ratio between the two peaks across each flyby. Each measurement is made by first taking an average across the whole energetic particle shadow and fitting and subtracting a Kappa distribution. The total flux of each peak is then estimated by manually fitting a Gaussian distribution. The ratio can then be calculated from these fits and the errors estimated by varying the manual fitting to find reasonable minimum and maximum fits.

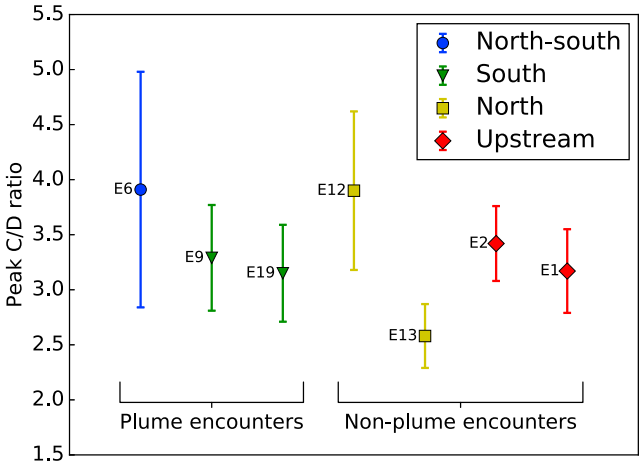

Figure 5. Ratio of Peaks C (16–30 eV) / D (30–60 eV) for a selection of flybys with different flyby geometries.

Figure 5 shows the results of calculating the Peak C/D ratios for a variety of Enceladus flybys, plotting them all sorted by flyby trajectory. The error on measuring the intensity of each peak is large, and there is no obvious relationship between plume encounter flybys and trajectories far from the plume.

For our analysis, we have scaled the modeled photoelectron production rate spectra (e.g., Figure 4) to the subtracted ELS data (Figures 3b and 3d) and shifted the spectra using potential estimates from the Radio and Plasma Wave Science instrument (RPWS).

Since we are not considering any transport and loss processes, we can qualitatively compare the ELS electron spectra and the modeled photoelectron production rate. We use CAPS-ELS data from the E9 and E19 Enceladus flybys

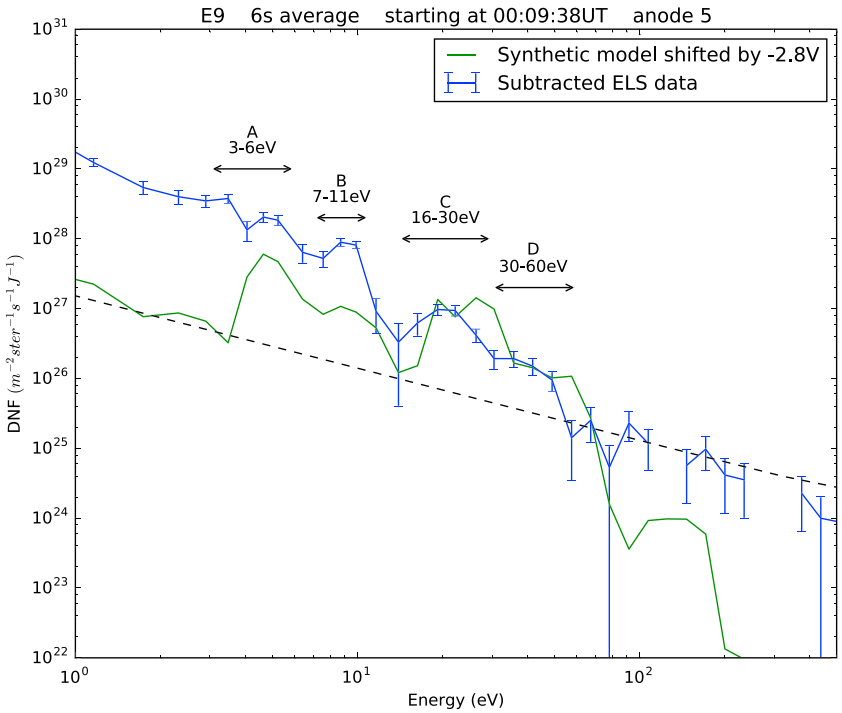

Figure 6. Kappa subtracted ELS data during E9 at 00:09:38 UT from anode 5 is shown in blue. Synthetic photoelectron production rate spectra shifted by RPWS spacecraft potential estimate and scaled to the ELS data is displayed in green. The dashed line indicates the single count level of ELS.

as they are the best examples of plume photoelectron observations made by ELS throughout the mission. Other flybys which also encounter the Enceladus plume are less suitable due to other factors such as instrument orientation (negative ions and dust are observed in the ram direction) and closest approach distance.

5.1. E9

Figure 6 shows the results of overlaying the synthetic photoelectron production spectrum onto the subtracted ELS data from E9. The data are a 6 s average (three sweeps) from ELS anode 5, centered on 00:09:38 UT. Qualitatively, we can see that shifting our model by the RPWS spacecraft potential estimate provides a reasonable fit to the subtracted ELS data. Peaks A, B, C, and D are all prominent in the subtracted data, while there is no obvious structure in the 100–200 eV range (Peak E) and most flux here is likely to be noise.

5.2. E19

Figure 7 shows the results of overlaying the synthetic photoelectron production spectrum onto the subtracted ELS data from E19. The data are a 4 s average (two sweeps) from anode 3 centered on 09:31:29 UT, near the center of the plume. We can again see that the result of potential shifting the model by the RPWS estimate provides us with a good fit to subtracted data. We again see evidence for peaks A, B, C, and D while any data in the range of E (100–200 eV) is likely noise.

The fact that the fluxes are at times higher in the subtracted data than in the model at energies $\lesssim$10 eV in both cases suggests that the Kappa fitting and subtraction may not be capturing the entire background population, and some magnetospheric electrons still remain. Unfortunately, the Kappa high-energy tail is relatively poorly constrained as the counts at energies $\gtrsim$100 eV are close to (or below) the single count noise level of the instrument.

It is likely that additional disagreements between the data and model are in part due to the affects of source, transport, and loss processes which are not considered. In the electron impact ionization process, a hot electron hits a neutral molecule and two electrons are emitted: a cold electron (a few eV) and a warm electron (energy lower than the original impacting electron). Compared to photoionization, the cross sections for electron impact ionization result in a much broader electron energy spectrum. Due to the relative lack of hot

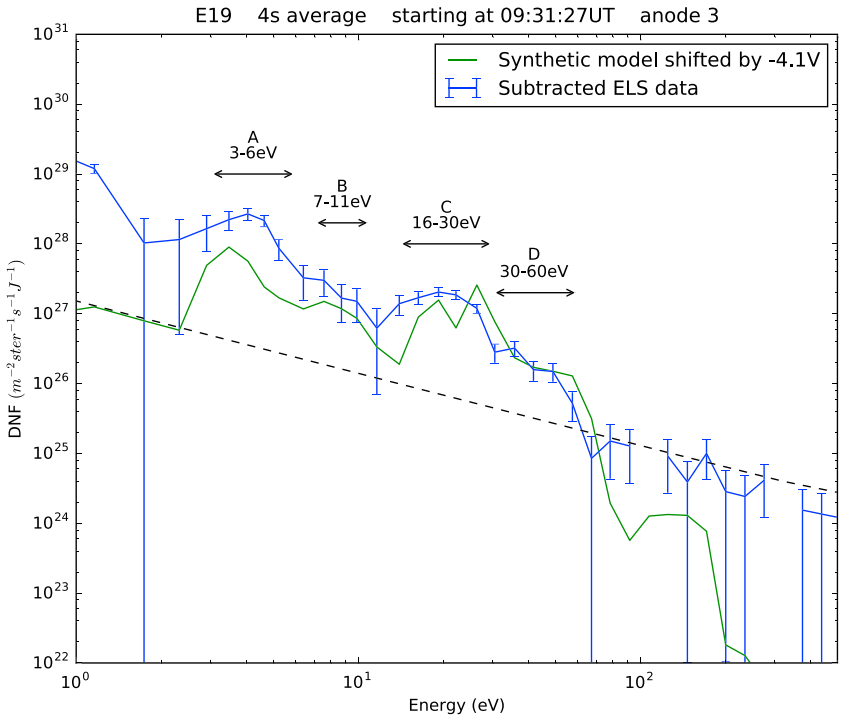

Figure 7. Kappa subtracted ELS data during E19 at 09:31:27 UT from anode 3 is shown in blue. Synthetic photoelectron production rate spectra shifted by RPWS spacecraft potential estimate and scaled to the ELS data are displayed in green. The dashed line indicates the single count level of ELS.

electrons in the energetic particle shadow and broad spectrum produced, we consider it unlikely that electron impact ionization affects the observed peak structure significantly even if the total flux contribution is large.

Although the model only considers photoelectron production rates, we can see strong evidence that the multiply peaked structure observed in the subtracted ELS data can be explained by photoelectrons produced in the plume neutrals surrounding Enceladus. There is evidence for Peaks A (3–6 eV), B (7–11 eV), C (16–30 eV), and D (30–60 eV) at both E9 and E19. There is also some evidence for Peak E at 100–200 eV in longer averages, though at much lower count rates and often close to the noise level of the instrument (not shown here).

6. Summary and Conclusions

The negatively charged particle environment near Enceladus consists of several populations: magnetospheric electrons, photoelectrons, cluster ions, and charged ice grains. Peaks at ≈16–30 eV and ≈30–60 eV have previously been identified using CAPS/ELS data both in the plume of Enceladus (Coates et al., 2013; Ozak et al., 2012) and the inner magnetosphere (Cravens et al., 2011; Schippers et al., 2009). We observe both of these populations unambiguously during all of the Enceladus flybys during which the instrument is oriented away from the ram direction. During ram-oriented flybys, we still see evidence of photoelectrons but much of the detail is obscured by negative ions and dust grain impacts.

By first subtracting the magnetospheric electron population, we have been able to identify a series of electron peaks in the low-energy range (<100 eV) of ELS electron spectra during Enceladus flybys E9 and E19. These peaks include previously unidentified structure at energies below ≈20 eV. By comparing the data to a synthetic photoelectron production model, we conclude that this structure can be explained by photoelectrons created by the photoionization of neutrals being emitted in the plumes of Enceladus.

We find that RPWS spacecraft potential estimates are sufficient to align the peaks predicted by the model and those revealed in the data using Kappa subtraction. Spacecraft potential estimates made using ELS data from Titan's ionosphere (Coates, Crary, Lewis, et al., 2007; Desai et al., 2017) and the inner magnetosphere (Schippers et al., 2009) have found differences between ELS and RPWS potentials of around −2 to 0.5 V. A possible explanation for this discrepancy is differential charging on the spacecraft caused by variations in the

conductivity of surfaces on different parts of the spacecraft (Crary et al., 2009). Due to the limited resolution of ELS and the broadness of these peaks in this environment, it is impossible using this method to conclude whether or not these differences exist for this data. With a more sophisticated model and better energy resolution, future missions may be able to take advantage of this technique to accurately assess the spacecraft potential using photoelectron peaks.

All of these photoelectrons being produced in the Enceladus plumes and surrounding neutral torus contribute to the total "hot" electron population. Using 3-D moment electron densities calculated using the method outlined in Lewis et al. (2008), we estimate that the "hot" (>15 eV) to "cold" (<15 eV) electron density ratio is ≈0.1–0.5%. This ratio is important for informing magnetospheric models, especially of the inner magnetosphere (e.g., Fleshman et al., 2012).

Acknowledgments
S. A. Taylor is supported by STFC Studentship 1440263. A. J. Coates, G. H. Jones, A. Wellbrock, and A. N. Fazakerley acknowledge support from the STFC consolidated grants to UCL-MSSL ST/K000977/1 and ST/N000722/1. We acknowledge funding from ESA via the UK Space Agency for the Cassini CAPS Operations team. Cassini CAPS and RPWS data are available from the NASA PDS (http://pds. nasa.gov/).

References

André, N., Blanc, M., Maurice, S., Schippers, P., Pallier, E., Gombosi, T. I., … Clarke, J. T. (2008). Identification of Saturn's magnetospheric regions and associated plasma processes: Synopsis of Cassini observations during orbit insertion. *Reviews of Geophysics*, *46*, RG4008. https://doi.org/10.1029/2007RG000238

Arridge, C. S., André, N., McAndrews, H. J., Bunce, E. J., Burger, M. H., Hansen, K. C., … Dougherty, M. K. (2011). Mapping magnetospheric equatorial regions at Saturn from Cassini prime mission observations. *Space Science Reviews*, *164*, 1–83. https://doi.org/10.1007/s11214-011-9850-4

Coates, A. J., Crary, F. J., Lewis, G. R., Young, D. T., Waite, J. H., & Sittler, E. C. (2007). Discovery of heavy negative ions in Titan's ionosphere. *Geophysical Research Letters*, *34*, L22103. https://doi.org/10.1029/2007GL030978

Coates, A. J., Crary, F. J., Young, D. T., Szego, K., Arridge, C. S., Bebesi, Z., … Hill, T. W. (2007). Ionospheric electrons in Titan's tail: Plasma structure during the Cassini T9 encounter. *Geophysical Research Letters*, *34*, L24S05. https://doi.org/10.1029/2007GL030919

Coates, A. J., Frahm, R. A., Linder, D. R., Kataria, D. O., Soobiah, Y., Collinson, G., … Grande, M. (2008). Ionospheric photoelectrons at Venus: Initial observations by ASPERA-4 ELS. *Planetary and Space Science*, *56*, 802–806. https://doi.org/10.1016/j.pss.2007.12.008

Coates, A. J., Johnstone, A. D., Sojka, J. J., & Wrenn, G. L. (1985). Ionospheric photoelectrons observed in the magnetosphere at distances up to 7 Earth radii. *Planetary and Space Science*, *33*, 1267–1275. https://doi.org/10.1016/0032-0633(85)90005-4

Coates, A. J., Jones, G. H., Lewis, G. R., Wellbrock, A., Young, D. T., Crary, F. J., … Hill, T. W. (2010). Negative ions in the Enceladus plume. *Icarus*, *206*, 618–622. https://doi.org/10.1016/j.icarus.2009.07.013

Coates, A. J., McAndrews, H. J., Rymer, A. M., Young, D. T., Crary, F. J., Maurice, S., … Lewis, G. R. (2005). Plasma electrons above Saturn's main rings: CAPS observations. *Geophysical Research Letters*, *32*, L14S09. https://doi.org/10.1029/2005GL022694

Coates, A. J., Tsang, S. M. E., Wellbrock, A., Frahm, R. A., Winningham, J. D., Barabash, S., … Crary, F. J. (2011). Ionospheric photoelectrons: Comparing Venus, Earth, Mars and Titan. *Planetary and Space Science*, *59*, 1019–1027. https://doi.org/10.1016/j.pss.2010.07.016

Coates, A. J., Wellbrock, A., Jones, G. H., Waite, J. H., Schippers, P., Thomsen, M. F., … Tokar, R. L. (2013). Photoelectrons in the Enceladus plume. *Journal of Geophysical Research: Space Physics*, *118*, 5099–5108. https://doi.org/10.1002/jgra.50495

Collier, M. R., & Hamilton, D. C. (1995). The relationship between kappa and temperature in energetic ion spectra at Jupiter. *Geophysical Research Letters*, *22*, 303–306. https://doi.org/10.1029/94GL02997

Cravens, T. E., Ozak, N., Richard, M. S., Campbell, M. E., Robertson, I. P., Perry, M., & Rymer, A. M. (2011). Electron energetics in the Enceladus torus. *Journal of Geophysical Research*, *116*, A09205. https://doi.org/10.1029/2011JA016498

Crary, F. J., Magee, B. A., Mandt, K., Waite, J. H., Westlake, J., & Young, D. T. (2009). Heavy ions, temperatures and winds in Titan's ionosphere: Combined Cassini CAPS and INMS observations. *Planetary and Space Science*, *57*, 1847–1856. https://doi.org/10.1016/j.pss.2009.09.006

Desai, R. T., Coates, A. J., Wellbrock, A., Vuitton, V., Crary, F. J., González-Caniulef, D., … Sittler, E. C. (2017). Carbon chain anions and the growth of complex organic molecules in Titan's ionosphere. *Astrophysical Journal Letters*, *844*, L18. https://doi.org/10.3847/2041-8213/aa7851

Dong, Y., Hill, T. W., & Ye, S.-Y. (2015). Characteristics of ice grains in the Enceladus plume from Cassini observations. *Journal of Geophysical Research: Space Physics*, *120*, 915–937. https://doi.org/10.1002/2014JA020288

Dougherty, M. K., Khurana, K. K., Neubauer, F. M., Russell, C. T., Saur, J., Leisner, J. S., & Burton, M. E. (2006). Identification of a dynamic atmosphere at Enceladus with the Cassini magnetometer. *Science*, *311*, 1406–1409. https://doi.org/10.1126/science.1120985

Esposito, L. W., Colwell, J. E., Larsen, K., McClintock, W. E., Stewart, A. I. F., Hallett, J. T., … Yung, Y. L. (2005). Ultraviolet imaging spectroscopy shows an active Saturnian system. *Science*, *307*, 1251–1255. https://doi.org/10.1126/science.1105606

Fleshman, B. L., Delamere, P. A., Bagenal, F., & Cassidy, T. (2012). The roles of charge exchange and dissociation in spreading Saturn's neutral clouds. *Journal of Geophysical Research*, *117*, E05007. https://doi.org/10.1029/2011JE003996

Frahm, R. A., Winningham, J. D., Sharber, J. R., Scherrer, J. R., Jeffers, S. J., Coates, A. J., … Dierker, C. (2006). Carbon dioxide photoelectron energy peaks at Mars. *Icarus*, *182*, 371–382. https://doi.org/10.1016/j.icarus.2006.01.014

Galand, M., Yelle, R. V., Coates, A. J., Backes, H., & Wahlund, J.-E. (2006). Electron temperature of Titan's sunlit ionosphere. *Geophysical Research Letters*, *33*, L21101. https://doi.org/10.1029/2006GL027488

Gibbons, J. D., & Chakraborti, S. (2011). *Nonparametric statistical inference* (pp. 977–979). Berlin, Heidelberg: Springer.

Hill, T. W., Thomsen, M. F., Tokar, R. L., Coates, A. J., Lewis, G. R., Young, D. T., … Horányi, M. (2012). Charged nanograins in the Enceladus plume. *Journal of Geophysical Research*, *117*, A05209. https://doi.org/10.1029/2011JA017218

Huebner, W. F., Keady, J. J., & Lyon, S. (1992). Solar photo rates for planetary atmospheres and atmospheric pollutants. *Astrophysics and Space Science*, *195*(1), 1–294. https://doi.org/10.1007/BF00644558

Jones, G. H., Arridge, C. S., Coates, A. J., Lewis, G. R., Kanani, S., Wellbrock, A., … Magee, B. A. (2009). Fine jet structure of electrically charged grains in Enceladus' plume. *Geophysical Research Letters*, *36*, L16204. https://doi.org/10.1029/2009GL038284

Jones, G. H., Roussos, E., Krupp, N., Paranicas, C., Woch, J., Lagg, A., … Dougherty, M. K. (2006). Enceladus' varying imprint on the magnetosphere of Saturn. *Science*, *311*, 1412–1415. https://doi.org/10.1126/science.1121011

Jurac, S., & Richardson, J. D. (2007). Neutral cloud interaction with Saturn's main rings. *Geophysical Research Letters*, *34*, L08102. https://doi.org/10.1029/2007GL029567

Krupp, N., Roussos, E., Lagg, A., Woch, J., Müller, A. L., Krimigis, S. M., … Sergis, N. (2009). Energetic particles in Saturn's magnetosphere during the Cassini nominal mission (July 2004–July 2008). *Planetary and Space Science*, *57*, 1754–1768. https://doi.org/10.1016/j.pss.2009.06.010

Lewis, G. R., André, N., Arridge, C. S., Coates, A. J., Gilbert, L. K., Linder, D. R., & Rymer, A. M. (2008). Derivation of density and temperature from the Cassini Huygens CAPS electron spectrometer. *Planetary and Space Science*, *56*, 901–912. https://doi.org/10.1016/j.pss.2007.12.017

Linder, D. R., Coates, A. J., Woodliffe, R. D., Alsop, C., Johnstone, A. D., Grande, M., … Young, D. T. (1998). The Cassini CAPS electron spectrometer. In R. F. Pfaff, J. E. Borovsky, & D. T. Young (Eds.), *American geophysical union geophysical monograph series* (Vol. 102, 257 pp.). Washington, DC: American Geophysical Union.

Mantas, G. P., & Hanson, W. B. (1979). Photoelectron fluxes in the Martian ionosphere. *Journal of Geophysical Research*, *84*, 369–385. https://doi.org/10.1029/JA084iA02p00369

Ozak, N., Cravens, T. E., Jones, G. H., Coates, A. J., & Robertson, I. P. (2012). Modeling of electron fluxes in the Enceladus plume. *Journal of Geophysical Research*, *117*, A06220. https://doi.org/10.1029/2011JA017497

Paranicas, C., Mitchell, D. G., Roussos, E., Kollmann, P., Krupp, N., Müller, A. L., … Johnson, R. E. (2010). Transport of energetic electrons into Saturn's inner magnetosphere. *Journal of Geophysical Research*, *115*, A09214. https://doi.org/10.1029/2010JA015853

Perry, M. E., Teolis, B., Smith, H. T., McNutt, R. L., Fletcher, G., Kasprzak, W., … Waite, J. H. (2010). Cassini INMS observations of neutral molecules in Saturn's E-ring. *Journal of Geophysical Research*, *115*, A10206. https://doi.org/10.1029/2010JA015248

Porco, C. C., Helfenstein, P., Thomas, P. C., Ingersoll, A. P., Wisdom, J., West, R., … Squyres, S. (2006). Cassini observes the active south pole of Enceladus. *Science*, *311*, 1393–1401. https://doi.org/10.1126/science.1123013

Rymer, A. M., Coates, A. J., Svenes, K., Abel, G. A., Linder, D. R., Narheim, B., … Young, D. T. (2001). Cassini plasma spectrometer electron spectrometer measurements during the Earth swing-by on August 18, 1999. *Journal of Geophysical Research*, *106*, 30,177–30,198. https://doi.org/10.1029/2001JA900087

Schippers, P., André, N., Johnson, R. E., Blanc, M., Dandouras, I., Coates, A. J., … Young, D. T. (2009). Identification of photoelectron energy peaks in Saturn's inner neutral torus. *Journal of Geophysical Research*, *114*, A12212. https://doi.org/10.1029/2009JA014368

Schippers, P., Blanc, M., André, N., Dandouras, I., Lewis, G. R., Gilbert, L. K., … Dougherty, M. K. (2008). Multi-instrument analysis of electron populations in Saturn's magnetosphere. *Journal of Geophysical Research*, *113*, A07208. https://doi.org/10.1029/2008JA013098

Spahn, F., Schmidt, J., Albers, N., Hörning, M., Makuch, M., Seiß, M., … Grün, E. (2006). Cassini dust measurements at Enceladus and implications for the origin of the E ring. *Science*, *311*, 1416–1418. https://doi.org/10.1126/science.1121375

Sprent, P., & Smeeton, N. C. (2016). *Applied nonparametric statistical methods*. Washington, DC: CRC Press.

Tokar, R. L., Johnson, R. E., Hill, T. W., Pontius, D. H., Kurth, W. S., Crary, F. J., … Gurnett, D. A. (2006). The interaction of the atmosphere of Enceladus with Saturn's plasma. *Science*, *311*, 1409–1412. https://doi.org/10.1126/science.1121061

Tokar, R. L., Johnson, R. E., Thomsen, M. F., Wilson, R. J., Young, D. T., Crary, F. J., … Paty, C. S. (2009). Cassini detection of Enceladus' cold water-group plume ionosphere. *Geophysical Research Letters*, *36*, L13203. https://doi.org/10.1029/2009GL038923

Vasyliunas, V. M. (1968). A survey of low-energy electrons in the evening sector of the magnetosphere with OGO 1 and OGO 3. *Journal of Geophysical Research*, *73*, 2839–2884. https://doi.org/10.1029/JA073i009p02839

Waite, J. H., Combi, M. R., Ip, W.-H., Cravens, T. E., McNutt, R. L., Kasprzak, W., … Tseng, W.-L. (2006). Cassini ion and neutral mass spectrometer: Enceladus plume composition and structure. *Science*, *311*, 1419–1422. https://doi.org/10.1126/science.1121290

Waite, J. H., Glein, C. R., Perryman, R. S., Teolis, B. D., Magee, B. A., Miller, G., … Bolton, S. J. (2017). Cassini finds molecular hydrogen in the Enceladus plume: Evidence for hydrothermal processes. *Science*, *356*(6334), 155–159. https://doi.org/10.1126/science.aai8703

Wellbrock, A., Coates, A. J., Sillanpää, I., Jones, G. H., Arridge, C. S., Lewis, G. R., … Aylward, A. D. (2012). Cassini observations of ionospheric photoelectrons at large distances from Titan: Implications for Titan's exospheric environment and magnetic tail. *Journal of Geophysical Research*, *117*, A03216. https://doi.org/10.1029/2011JA017113

Young, D. T., Berthelier, J. J., Blanc, M., Burch, J. L., Coates, A. J., Goldstein, R., … Zinsmeyer, C. (2004). Cassini plasma spectrometer investigation. *Space Science Reviews*, *114*, 1–112. https://doi.org/10.1007/s11214-004-1406-4

Erratum

In the originally published version of this article, references to the 'rate coefficient, *k*' in the second paragraph in Section 4: Model had been erroneously included and were deleted from the text and corresponding equation. The rare-coefficient, *k*, has not been referenced elsewhere in the text, the science is unaffected, and the present version may be considered the authoritative version of record.